CrossMark

J. Fluid Mech. (2017), *vol.* 818, *pp.* 184–204. © Cambridge University Press 2017
doi:10.1017/jfm.2017.47

Normalized dissipation rate in a moderate Taylor Reynolds number flow

Alejandro J. Puga[1,†] **and John C. LaRue**[1]

[1]Department of Mechanical and Aerospace Engineering, University of California, Irvine, CA 92697, USA

(Received 28 January 2016; revised 18 January 2017; accepted 19 January 2017;
first published online 29 March 2017)

Time-resolved velocity measurements are obtained using a hot-wire in a nearly homogeneous and isotropic flow downstream of an active grid for a range of Taylor Reynolds numbers from 191 to 659. It is found that the dimensionless dissipation rate, C_ϵ, is nearly a constant for sufficiently high values of Taylor Reynolds number, R_{λ,u_q}, and is approximately equal to 0.87. This value is approximately 5 % less than the value reported by Bos *et al.* (*Phys. Fluids*, vol. 19 (4), 2007, 045101), which is obtained using DNS/LES (direct numerical simulation combined with large eddy simulation) for decaying homogeneous and isotropic turbulence, and is in excellent agreement with the active grid experiment of Thormann & Meneveau (*Phys. Fluids*, vol. 26 (2), 2014, 025112.). The results presented herein show that deviation from isotropy may cause inconsistencies in the computation of C_ϵ. As a result, it is suggested that the velocity scale be the square root of the turbulence kinetic energy. The integral length scale measurements obtained from the longitudinal velocity correlation are in close agreement with the integral length scale measured from the peak of the energy spectrum, $\kappa E_{11}(\kappa)$, where κ is the wavenumber and $E_{11}(\kappa)$ is the one-dimensional power spectrum of the downstream velocity.

Key words: homogeneous turbulence, isotropic turbulence, turbulent flows

1. Background

One of the most fundamental concepts in turbulent flows is that the dissipation rate, ϵ, of turbulence kinetic energy, represented by $\mathcal{U}^2$, of the large eddies of scale l must be proportional to the time scale of those eddies, $l/\mathcal{U}$, where $\mathcal{U}$ is the velocity scale corresponding to the large-scale structures. Based on that reasoning, an estimate for the dissipation is that

$$\epsilon = C_\epsilon \mathcal{U}^3/l, \tag{1.1}$$

where C_ϵ is a proportionality constant expected to be of order unity. While it is possible to find the constant C_ϵ by determining values of ϵ, $\mathcal{U}$ and l, Tennekes & Lumley (1972) present an alternative expression where C_ϵ can be determined as

$$R_l = (C_\epsilon/15)R_\lambda^2, \tag{1.2}$$

† Email address for correspondence: apuga@uci.edu

https://doi.org/10.1017/jfm.2017.47 Published online by Cambridge University Press

where R_l is the Reynolds number based on the length scale, l, and is defined as

$$R_l = \frac{\mathcal{U} l}{\nu}, \tag{1.3}$$

where ν is the kinematic viscosity. R_λ is the Reynolds number based on the Taylor microscale, $\lambda \equiv \mathcal{U}^2/\overline{(\partial u/\partial x)^2}$ where the overbar denotes time average, and is defined as

$$R_\lambda = \frac{\mathcal{U}\lambda}{\nu}. \tag{1.4}$$

There have been many studies that have focused on finding the normalized dissipation rate coefficient experimentally and numerically. Vassilicos (2015) provides an insightful and comprehensive review on the subject of normalized dissipation rate. Experimental studies in shear flows have been reported by Sreenivasan (1984), Pearson, Krogstad & Water (2002), Burattini, Lavoie & Antonia (2005), wake flows reported by Antonia & Pearson (2000), Pearson *et al.* (2002), jet flows reported by Boffetta & Romano (2002), Mazellier & Vassilicos (2008) and grid flows, including standard (Burattini *et al.* 2005; Krogstad & Davidson 2011; Valente & Vassilicos 2011; Isaza, Salazar & Warhaft 2014), fractal (Seoud & Vassilicos 2007; Mazellier & Vassilicos 2008; Valente & Vassilicos 2011; Hearst & Lavoie 2014; Valente & Vassilicos 2014) and active grids by Mydlarski & Warhaft (1996), Pearson *et al.* (2002), Burattini *et al.* (2005). While some studies are in agreement with the Richardson–Kolmogorov phenomenology and have found evidence to support the constancy of C_ϵ with respect to R_λ, others have found that the value of C_ϵ, whether constant or not, is not universal, but a function of boundary/initial conditions (see Vassilicos (2015) for a comprehensive discussion).

Numerical studies have been performed using both forced (Wang *et al.* 1996; Yeung & Zhou 1997; Sreenivasan 1998; Cao, Chen & Doolen 1999; Ishihara & Kaneda 2003; Kaneda *et al.* 2003; Bos, Shao & Bertoglio 2007; Goto & Vassilicos 2009) and decaying (Sreenivasan 1998; Burattini *et al.* 2005; Bos *et al.* 2007) isotropic and homogeneous turbulence. Similar to experimental studies, values for C_ϵ are not in agreement. Bos *et al.* (2007) show that the value of C_ϵ in forced isotropic turbulence must be lower than that of decaying isotropic turbulence due to the time required for the turbulence kinetic energy to transfer from the large to small scales. The physical reasoning given is that for decaying turbulence at a particular point in time, the energy being dissipated is equal (or proportional) to the energy that populated the large scales at a previous point in time that is dependent on the time scale related to the energy transfer and not to the energy in the large scales at the present time (cf. Bos *et al.* 2007). This implies that decaying turbulence should not be directly compared to non-decaying, forced turbulence as well as non-homogeneous, non-isotropic turbulence due to the non-zero turbulence production present in those flows.

The simplest way to produce nearly homogeneous and isotropic turbulence in a wind tunnel is by use of a stationary, bi-plane grid. This method, however, does not typically produce high R_λ flows where a sufficiently large enough separation of the large and small scales is present. More recently, researchers have developed fractal grids that produce turbulence with higher R_λ values. The turbulence produced by fractal grids, however, is reported to decay much faster than standard grid turbulence as an exponential decay (Hurst & Vassilicos 2007; Mazellier & Vassilicos 2010) or possibly a power law with a large decay coefficient (Valente & Vassilicos 2011). It is shown that in the near field ($x/L_o \leqslant 20$ where L_o is the largest fractal dimension

https://doi.org/10.1017/jfm.2017.47 Published online by Cambridge University Press

on the grid), l/λ, where l is the integral length scale, is a constant with respect to downstream position or R_λ, which implies that C_ϵ must decay with increasing R_λ since

$$l/\lambda = \frac{C_\epsilon}{15} R_\lambda. \tag{1.5}$$

Although Seoud & Vassilicos (2007) and Mazellier & Vassilicos (2010) find that the flow in the near field of their fractal grids is homogeneous in the mean flow and turbulence profiles, Valente & Vassilicos (2011) find that there is still significant transverse turbulent transport of turbulence kinetic energy and pressure. Hearst & Lavoie (2014) show that in the far field ($x/L_o \geqslant 20$) of fractal grids, the flow appears to follow traditional grid flows with varying l/λ such that C_ϵ is constant. Isaza *et al.* (2014) confirm the findings of Valente & Vassilicos (2014) that show the turbulence decay rate in the near field of a conventional, bi-plane grid ($x/M = 6$ to $x/M = 12$) departs from classical turbulence and is similar to what has been reported for the near field of fractal grids. The data obtained in the present experiment are in the far field of an active grid and will be compared to the far field of other grid experiments (conventional, fractal and active).

The first step in the determination of C_ϵ is to determine the values for the characteristic velocity and length scale as well as the dissipation rate. Traditionally, the velocity scale that has been used is

$$\mathcal{U} \equiv \overline{u^2}^{1/2}. \tag{1.6}$$

An alternative velocity scale is

$$\mathcal{U} \equiv (q/3)^{1/2}, \tag{1.7}$$

where $q = \overline{u^2} + \overline{v^2} + \overline{w^2}$ and u, v and w are the velocity components in the three coordinate directions. If the flow is isotropic, the two scales are the same but if there is a departure from isotropy, the two scales would lead to different values for the normalized dissipation rate.

As suggested by Burattini *et al.* (2005), the method used to measure the large-scale structure, hereafter referred to as the integral length scale, should be taken into account when assessing the behaviour of C_ϵ. In this study, the integral length scale is measured using two independent methods and their effect on C_ϵ is investigated.

The integral length scale, l, is determined by integrating the time autocorrelation of the downstream velocity. For this approach, the integral length scale is determined from the integral time scale, which is formally defined as

$$T = \int_0^\infty \rho(u(x,t)u(x,t+\tau))\,\mathrm{d}\tau, \tag{1.8}$$

where

$$\rho(u(x,t)u(x,t+\tau)) = \frac{\overline{u(x,t)u(x,t+\tau)}}{\overline{u(x,t)^2}}, \tag{1.9}$$

and the integral length scale is defined as

$$l \equiv l_a = \overline{U}T, \tag{1.10}$$

where l_a is the integral length scale measured using the autocorrelation method and $\overline{U}$ is the mean speed. In practice, the integral in (1.8) is evaluated to the first zero

https://doi.org/10.1017/jfm.2017.47 Published online by Cambridge University Press

crossing to circumvent the possibility that low wavenumber unsteadiness could cause the autocorrelation to not reach zero at large time separations (Burattini *et al.* 2005).

If the spatial correlation of the downstream velocity in the downstream direction, i.e.

$$\rho(u(x,t)u(x+\delta x,t)) = \frac{\overline{u(x,t)u(x+\delta x,t)}}{\overline{u(x,t)^2}} \tag{1.11}$$

has an exponential decay with δx, then the integral length scale has been shown to correspond to the wavenumber of the peak of the energy spectrum, $\kappa E_{11}(\kappa)$, where κ is the wavenumber and $E_{11}(\kappa)$ is the one-dimensional power spectrum of the downstream velocity (cf. Webb 1955). In this approach,

$$l \equiv l_s = 1/\kappa_n, \tag{1.12}$$

where l_s is the integral length scale measured using the spectrum method and κ_n is the wavenumber location of the peak of the energy spectrum. Pearson *et al.* (2002) use this integral scale definition to collapse C_ϵ data for several experiments. However, Burattini *et al.* (2005) show that l_s and l_a are only interchangeable for flows where $E_{11}(\kappa) \sim \kappa^2$ as $\kappa \to 0$.

The dissipation is determined using the variance of the temporal velocity derivative, Taylor's hypothesis and the assumption of local isotropy and is defined as

$$\epsilon = 15\nu\overline{\left(\frac{\partial u}{\partial x}\right)^2} = \frac{15\nu}{\overline{U}^2}\overline{\left(\frac{\partial u}{\partial t}\right)^2}. \tag{1.13}$$

Due to the relatively high turbulence intensities (defined as $\overline{u^2}^{1/2}/\overline{U}$) of as high as 11 % observed in the study presented herein, the validity of Taylor's hypothesis must be investigated to ensure proper space–time conversion or a correction must be employed if deemed necessary. These corrections are motivated by the fact that Taylor's hypothesis may not be accurate in flows with large turbulence intensities due to the breakdown of the frozen-turbulence assumption. Champagne (1978) demonstrates that in an inhomogeneous flow, which is more restrictive than a homogeneous flow, with an intensity of 9 %, Taylor's hypothesis can be used to accurately determine the spatial derivative from the time derivative if the flow is locally isotropic. Since the flow presented herein is nearly homogeneous and locally isotropic, equation (1.13) is used to determine the dissipation rate.

The goals of the study presented herein are: (i) to determine the value for C_ϵ based on (1.1) and (1.2) as a function of R_λ; (ii) to determine the value of R_λ where C_ϵ becomes a constant, defined as $C_{\epsilon,\infty}$; (iii) to determine the effect on the value of $C_{\epsilon,\infty}$ using the two velocity scales defined in (1.6) and (1.7); (iv) to compare the values of R_λ where C_ϵ becomes a constant and the value of $C_{\epsilon,\infty}$ to those of previous studies. An additional goal of the present study is to provide a comparison of the measures of l_a and l_s as defined in (1.12) and (1.10).

2. Experimental set-up

2.1. *Flow facilities*

The flow facility used for this experiment is the closed-return wind tunnel at the University of California, Irvine. The tunnel has a rectangular test section that is 0.91 m tall, 0.61 m wide, 6.71 m long and is preceded by a contraction section with

https://doi.org/10.1017/jfm.2017.47 Published online by Cambridge University Press

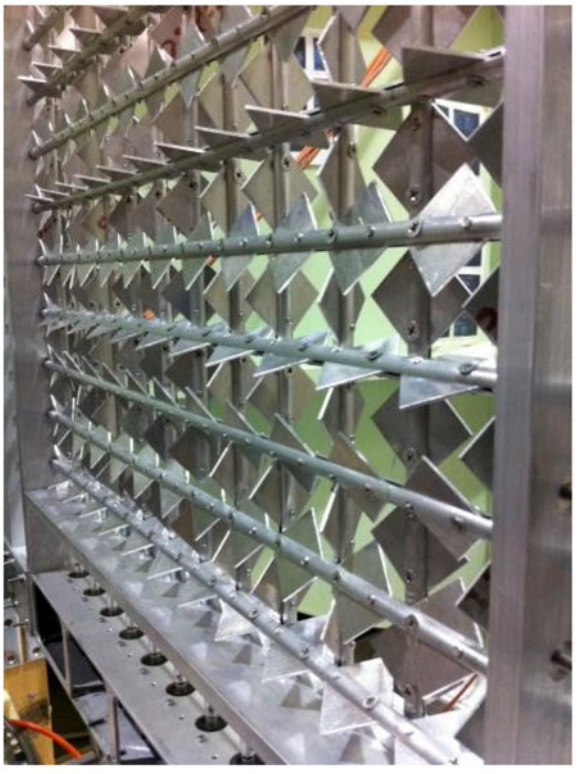


FIGURE 1. (Colour online) Image of the turbulence-generating active grid.

an area reduction ratio of 9.36. The ceiling and floor of the test section diverge to compensate for boundary layer growth and, thereby minimizing the mean velocity variation in the downstream direction. The high intensity, nearly homogeneous and isotropic flow is produced by means of an active, turbulence-generating grid, which is based on the initial design of Makita & Sassa (1991) as implemented by Mydlarski & Warhaft (1996).

2.2. *Active grid*

The active grid consists of an aluminium frame that holds 18 horizontal and 12 vertical cylindrical rods to form a square mesh, which can be seen in figure 1. The rods measure 9.5 mm in diameter and are spaced 50.8 mm apart. Hereafter, the rod spacing is referred to as M. Diamond-shaped flaps measuring 33 mm on a side are centre mounted along a 1.6 mm slit down the centre of each rod. The rod ends are placed in an oil-impregnated brass sleeve bearing that allows the rods to rotate smoothly. Each rod is attached to a high torque Anaheim Automation 17MD102S stepper motor that has a resolution of 200 steps per revolution and is mounted inside the hollow outer frame.

Two independent Parallax ProtoBoards, each capable of controlling 15 motors, are used to control the rotation speed and direction of rotation. If the controller is programmed to provide a fixed rotation rate and direction to the motors, the velocity power spectra will have a large relative peak that is centred at twice the rotation rate.

https://doi.org/10.1017/jfm.2017.47 Published online by Cambridge University Press

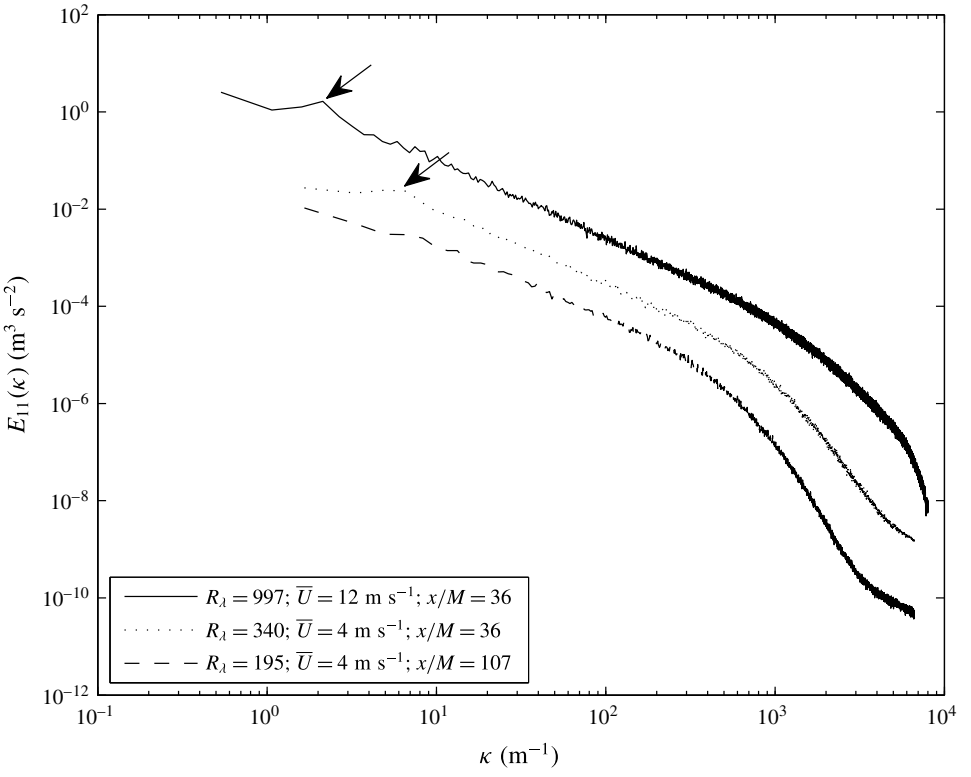


FIGURE 2. Velocity power spectra obtained at $x/M = 36$ and $x/M = 107$. Arrows denote the relative peaks at wavenumber locations corresponding to a frequency equal to twice the rotation rate of the active grid rods. The presence of the peaks cause an error of less than 1 % in $\overline{u^2}^{1/2}$.

Therefore, to minimize the effect of this peak, the mean rotation rate is set to two revolutions per second and the motor rotation rates are programmed to vary $\pm 25\,\%$ relative to the mean rotation rate. The direction of rotation along with the rotation rates are programmed to change every 125–325 ms. Note that all of the motors controlled by the same microcontroller will be assigned a new speed and direction at the same time.

While randomizing the grid parameters reduces the relative peak in the velocity power spectrum as shown by Hearst & Lavoie (2015), it is not completely eliminated as can be seen in figure 2, which shows velocity power spectra with mean velocities of 4 and 12 m s^{-1} at $x/M = 36$ and $x/M = 107$. Note that in order to reduce noise, spectra are computed from the average of 120 data sets each 1 s in length. It is found that the relative peak becomes more pronounced as the mean velocity increases or distance from the grid decreases but, at most, has a magnitude of a fraction of a decade. Integration of the power spectra to determine the relative contribution of the peak to the measured velocity variance indicates a contribution of less than 1 %. Due to the small size of the peak and relatively small contribution to the measured velocity variance, no corresponding correction is made. It is important to note that while the slope of the inertial subrange appears to be $-5/3$, the measured slope is less than

https://doi.org/10.1017/jfm.2017.47 Published online by Cambridge University Press

$-5/3$ and is a function of the Taylor Reynolds number which will be the topic of a future publication.

2.3. *Sensors*

The time-resolved velocity is measured using a standard, one-component hot-wire sensor. The hot-wire is fabricated from a 5.08 μm diameter Wollaston platinum wire manufactured by Sigmund Cohn. It is soldered to two stainless steel needles that are nickel plated to provide good electrical contact. The length of the platinum wire is nominally 1 mm, which yields a length to diameter ratio of approximately 200. This ratio matches the optimal ratio suggested by Azad (1993), which minimizes prong effects while maximizing spatial resolution. The data corresponding to 12 m s^{-1} are taken with a smaller hot-wire with a diameter of 1.27 μm and a sensing length of 0.4 mm. The 5.08 μm diameter hot-wire sensor is powered by an AA Labs System model AN-1005 constant temperature anemometer (CTA) with an overheat ratio of 1.75, which corresponds to a wire temperature of 249.9 °C. A pulse response test indicates that the frequency response of the sensor is about 30 kHz at 18 m s^{-1}. The 1.27 μm diameter hot-wire sensor is powered by a custom-built CTA system with an overheat ratio of 1.75 corresponding to a wire temperature of 243.1 °C. A pulse response test on the shorter hot-wire indicates that the frequency response of the sensor is approximately 20 kHz at 24 m s^{-1}. The wire temperature (T_w) is determined experimentally to within 1 °C by varying the speed from 2 to 20 m s^{-1} and varying temperature from 20 °C to 100 °C in a laminar calibration jet. This procedure will be discussed in detail in the calibration procedure section. Sensors are calibrated for T_w only a few times during the course of an experiment, however, a velocity calibration is obtained at the start and end of each data collection period. If the statistics of interest vary more than 1 % when analysed using the calibration coefficients found before and after the experiment, the corresponding data are discarded.

A X-wire is used to obtain time-resolved velocity measurements of two components (u and v) of velocity simultaneously. The sensor is rotated by 90° to obtain the third component of velocity, w. The X-wire is manufactured by Auspex with two 5.08 μm diameter tungsten wires that are spaced 1 mm apart with a sensing length of about 1 mm. The ends of the sensing wire are copper plated to mitigate thermal prong effects. A pulse response test obtained at 10 m s^{-1} shows that the frequency response of each wire is 22–25 kHz. Details on the X-wire and its calibration can be found in Nguyen (2015). However, for completeness, the calibration and velocity determination is briefly described in appendix A. Due to the large wire separation in the X-wire relative to the Kolmogorov length scale, the one-component hot-wire is used to measure dissipation rate. The purpose of the X-wire is primarily to measure $(\overline{u^2})^{1/2}$, $(\overline{v^2})^{1/2}$ and $(\overline{w^2})^{1/2}$ in order to determine the large-scale anisotropies. Due to the large relative Taylor Reynolds number, it is expected that the small dissipative scales are isotropic even if the large scales are not.

A reference mean velocity is obtained using a Pitot-static tube connected to an MKS Baratron Model 698A11TRE differential pressure transducer. The maximum difference between the mean velocity obtained using the Pitot-static tube and the hot-wire is less than 2 %. The mean temperature is measured using a platinum resistance thermometer (PRT) manufactured by Omega Engineering. It is connected to a custom-made Wheatstone bridge based on an Analog Devices 5B34-01 isolated linearized input module. The PRT is mounted 5 cm away from the hot-wire and is used to correct the hot-wire signal for mean gas temperature variation.

https://doi.org/10.1017/jfm.2017.47 Published online by Cambridge University Press

The Kolmogorov length scale (η) for the flow presented herein varies from 0.14 mm to 0.5 mm and, therefore, effects of spatial averaging are investigated for both the 1 mm and 0.4 mm wires. Wyngaard (1968) proposes a correction for the velocity and derivative spectra taken from hot wires that spatially average over multiple Kolmogorov scales. When this correction is implemented, the root-mean-square (r.m.s.) of velocity is found to be less than 0.5 % in error with the 1 mm long sensor and less than 0.2 % in error for the 0.4 mm long sensor for the worst cases. For that reason, no correction due to spatial averaging is made for the velocity spectrum or the computation of $\overline{u^2}^{1/2}$. Wyngaard's correction shows a correction in the derivative signal of up to 10 % for the 1 mm long wire and up to 4 % correction for the 0.4 mm long wire at locations where the Kolmogorov length scale is the smallest. For this reason, Wyngaard's correction is applied to the derivative spectra and the derivative r.m.s. accordingly. Furthermore, it is found that the noise in the derivative signal causes an error in the derivative r.m.s. that varies from 1 % to 3 %. The noise is removed from the derivative spectrum and a corrected derivative r.m.s. value is computed as suggested by Valente & Vassilicos (2014).

2.4. *Signal conditioning*

The voltage output from the CTA is filtered using an analogue, low pass, 4-pole Butterworth filter which incorporates a Frequency Devices (744PB-4) module. The filter has an insignificant amount of droop in the pass band up to 2/3 of the corner frequency, therefore, the corner frequency is set to 1.65 times higher than the frequency at which the signal reaches the noise level to ensure that the entire turbulent signal is not affected by the filter. Even though the filters are set to a higher than ideal corner frequency, the increased noise allowed to pass through increases the signal r.m.s. by less than 2 % for the majority of the data collected. The signal then goes through a custom-built, 3-stage amplifier that can both amplify and offset the signal to ensure that the majority of the dynamic range of the analogue to digital converter is used. The frequency response of the amplifier is flat to approximately 70 kHz. Next, the signal passes through a voltage divider that can either pass the signal unattenuated or attenuate it by 2/3. The voltage divider is used in combination with the amplifier to increase the signal to noise ratio. An analogue, low noise differentiator is used to provide the time derivative of the hot-wire signal. The bandwidth of the differentiator is approximately 18 kHz.

All signals are digitized using a 16-bit Measurement Computing Corp. 1608-HS analogue to digital converter with 8 differential analogue inputs that have an operational input range of ± 10 V and a maximum sampling rate of 250 kS s^{-1} per channel. The signal is transferred to a personal computer running Windows 7 via USB where the data are recorded and analysed using LabView2015.

2.5. *Calibration procedure*

The calibration equation for the hot-wire is based on a modified form of King's law:

$$E_{HW}^2 = (A_{HW} + B_{HW}\overline{U}^n)(T_w - T_g), \tag{2.1}$$

where E_{HW} is the voltage from the anemometer, $\overline{U}$ is the mean velocity, T_w is the wire temperature, T_g is the gas temperature and A_{HW} and B_{HW} are the calibration coefficients. As suggested by Bruun (1995), the value for the exponent, n, is determined using the calibration data and is not assumed to be 0.45. Based on

https://doi.org/10.1017/jfm.2017.47 Published online by Cambridge University Press

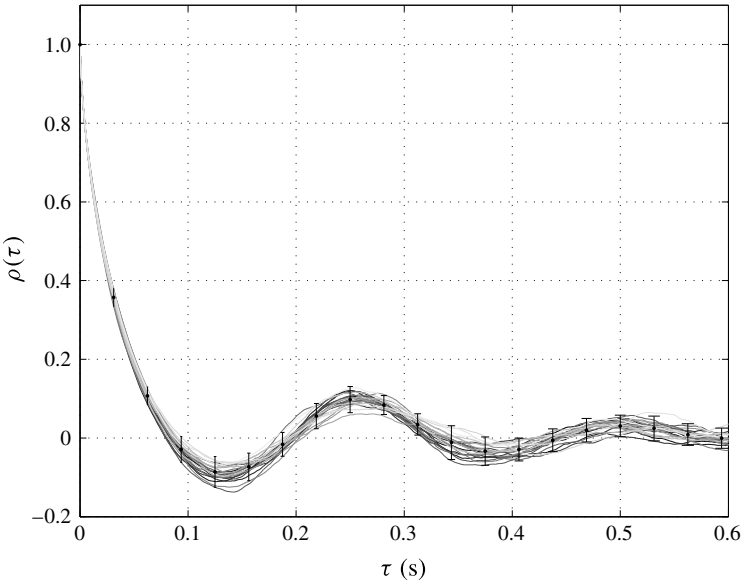


FIGURE 3. 23 autocorrelations taken at $\overline{U} = 8$ m s^{-1} and $x/M = 35$. The dots represent the local ensemble average of the autocorrelation and the error bars represent the scatter of the autocorrelation ($2\rho_{rms}$).

the fact that $E_{HW}^2/(T_w - T_g)$ is linearly related to $\overline{U}^n$, appropriate values of T_w and n are found that minimize the nonlinearity. For the current study, T_w and n are 249.9 °C and 0.403, respectively.

The next step in the calibration is carried out in the wind tunnel and is performed both before (pre-calibration) and after (post-calibration) a data collection period. For both the pre- and post-calibration, the gas temperature is measured using a PRT and the mean velocity is measured using the MKS Baratron and a Pitot-static tube. In this step, the velocity is varied over a range from 2 to 20 m s^{-1} and the wire temperature, T_w, and the velocity exponent, n, are assumed to remain equal to the values found in the previous step of the calibration. Data are only presented when the application of the pre- and post-calibration lead to less than a 1 % variation in the statistical values of interest.

3. Analysis procedure

3.1. *Integral length scale based on the autocorrelation*

The integral length scale can be determined by integrating the spatial autocorrelation of the downstream velocity. However, in practice, a 1-point correlation in time is more easily obtained and transformed to a spatial correlation as shown in (1.8)–(1.10). Nobach & Tropea (2012) compare a 2-point longitudinal spatial correlation taken with a laser Doppler anemometry (LDA) system to a 1-point time correlation. They find that the temporal correlation can be accurately transformed into the spatial correlation for flows with turbulence intensities of up to 25 % and, hence, l_a can be determined accurately using (1.10).

One challenge in determining a unique value for the integral length scale using this method is that the autocorrelation for a finite time sample varies in value at different time shifts, τ. For example, figures 3 and 4 show 23 autocorrelation curves

https://doi.org/10.1017/jfm.2017.47 Published online by Cambridge University Press

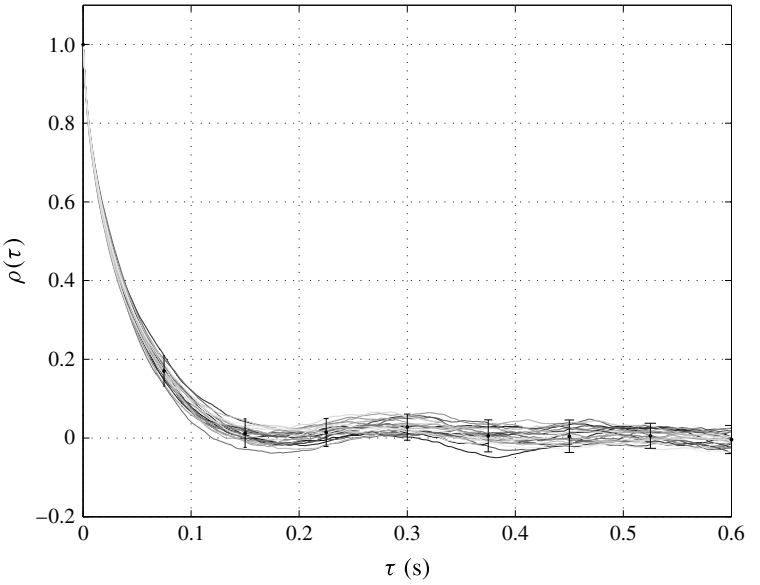


FIGURE 4. 23 autocorrelations taken at $\overline{U} = 4$ m s^{-1} and $x/M = 60$. The dots represent the local ensemble average of the autocorrelation and the error bars represent the scatter of the autocorrelation ($2\rho_{rms}$).

taken at 8 m s^{-1} and $x/M = 35$ and at 4 m s^{-1} and $x/M = 60$, respectively. The error bars shown on the plot represent ± 2 standard deviations (ρ_{rms}) from the mean normalized autocorrelation value as a function of time. Formally, the integral time scale is computed by integrating the autocorrelation to an infinite time as shown in (1.8). However, in practice, the integral time scale is determined by integrating the autocorrelation to the time corresponding to the first zero crossing. The variation in the autocorrelations leads to a variation in the value of the time corresponding to the first zero crossing. For the autocorrelations shown in figure 3, that variation in the zero crossing time has little effect on the value of the integral time scale with an uncertainty of less than 3 %. However, as shown in figure 4, the variability in the value of the autocorrelation can have a significant effect on the values of the time of the first zero crossing and also on the value of the integral time scale, in this case, the variation is 16 %.

To minimize the effect of the variability in the values of the autocorrelation and the variability in the value of the first zero crossing time, a modified version of (1.8) is employed where

$$T_o = \int_0^{\tau_o} \rho(u(x, t)u(x, t+\tau))\,\mathrm{d}\tau, \tag{3.1}$$

where

$$\tau_o \equiv \tau(\rho(\tau) = 0 + \delta), \tag{3.2}$$

where δ is twice the r.m.s. of the fluctuation of the correlation.

For all mean speeds and downstream positions, $\delta = 0.03 \pm 0.0053$. When the modified definition of the zero crossing time as shown in (3.2) is used, the uncertainty in the integral length scale from the autocorrelations shown in figure 4 decreases from 16 % to 6 %. For autocorrelations similar in structure to those shown in figure 3, the

https://doi.org/10.1017/jfm.2017.47 Published online by Cambridge University Press

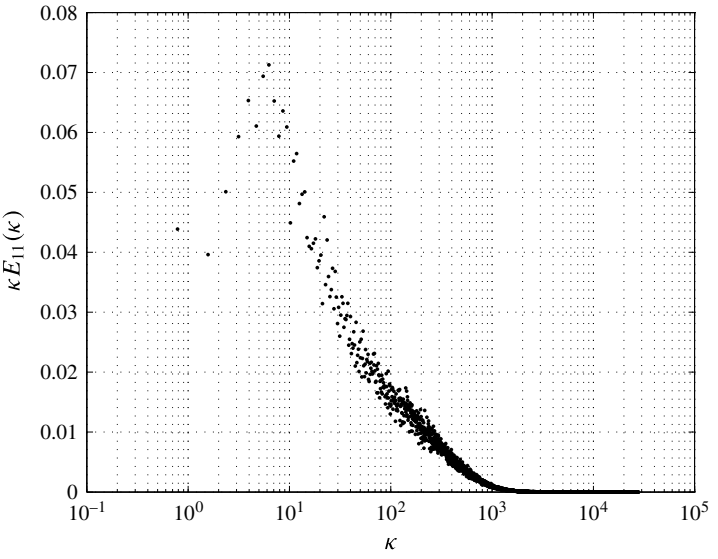


FIGURE 5. Energy spectrum ($\kappa E_{11}(\kappa)$) taken at 8.01 m s^{-1} and $x/M = 142.5$ exhibiting a clear spectral peak used to compute the integral scale, l_s.

use of τ_o as defined in (3.2) leads to less than a 1 % change in the integral time scale when compared to the value obtained using $\tau_o \equiv \tau(\rho(\tau) = 0)$. A small number of autocorrelations whose first minimum does not cross zero even with the δ correction are omitted.

As presented in a previous section, the velocity power spectrum corresponding to higher mean speeds and at close proximity to the active grid have a relative peak at a frequency equal to twice the mean rotation rate. As noted by Tennekes & Lumley (1972), a spike of finite width in the spectrum generates decaying oscillations of wavelength $2\pi/\kappa$ in the correlation and corresponds to the oscillations seen in the autocorrelation for longer time separations in figure 3.

3.2. *Integral length scale based on the spectral method*

As noted in the Background section, the integral length scale has been shown (Webb 1955) to correspond to the peak of the energy spectrum, $\kappa E_{11}(\kappa)$, for exponentially decaying autocorrelations. In this study, the autocorrelations do not have an exponential decay. Thus, there is some inherent uncertainty in the determination of the integral length scale using this approach. Furthermore, the relative peak in the power spectrum corresponding to the rod rotation of the active grid can obscure the location of the peak that corresponds to the large-scale structure. For example, a sample energy spectrum measured at a mean speed of 8.01 m s^{-1} at $x/M = 142.5$ is shown in figure 5 where the peak occurs at a wavenumber of 6.2 m^{-1}, which corresponds to a frequency of 7.9 Hz. However, for some combinations of mean speed and downstream locations, e.g. at 11.7 m s^{-1} and $x/M = 38$, as shown in figure 6, the peak in the energy spectrum occurs at a wavenumber of 2.1 m^{-1} with a corresponding frequency of 4 Hz, which is equal to twice the rotation rate of the grid. Thus, for this study, it is only possible to obtain the integral length scale using the peak of the energy spectrum at certain downstream locations.

https://doi.org/10.1017/jfm.2017.47 Published online by Cambridge University Press

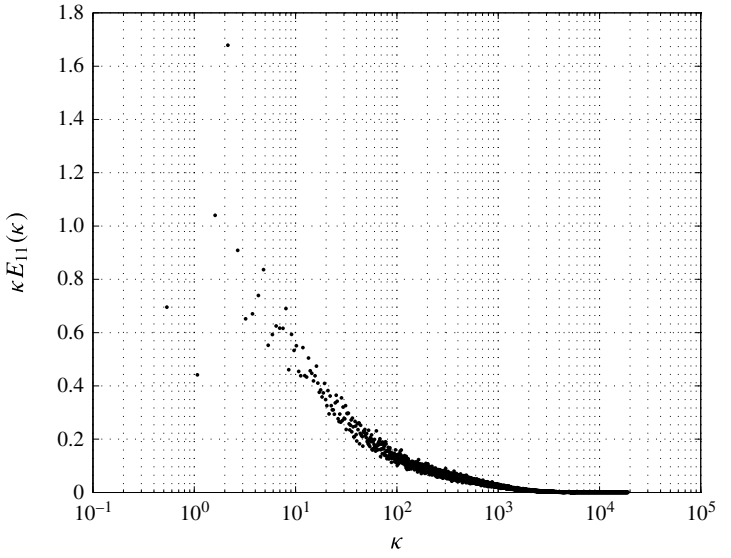


FIGURE 6. Energy spectrum ($\kappa E_{11}(\kappa)$) taken at 11.7 m s^{-1} and $x/M = 38$ and contains a relative peak at 4 Hz that obscures the spectral peak needed to find the integral scale, l_s.

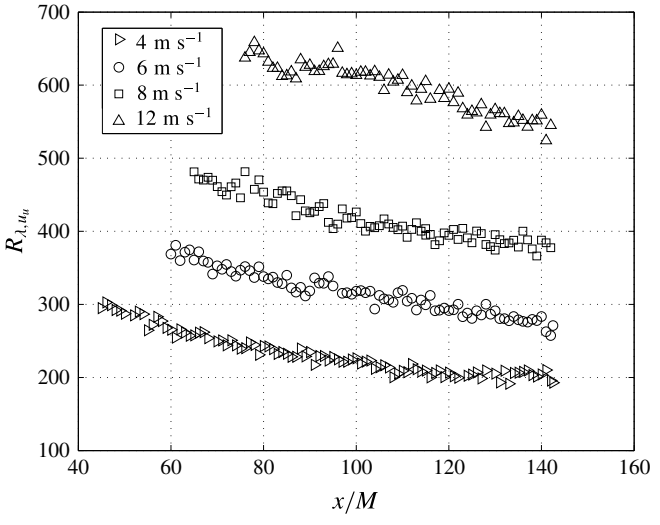


FIGURE 7. Comparison of R_{λ,u_u} as a function of x/M for 4, 6, 8 and 12 m s^{-1}.

4. Results

An R_λ range of 191–659 is achieved by varying mean speed ($\overline{U}$) and downstream location from the active grid (x/M). The mean velocities, range of downstream positions and corresponding Taylor Reynolds number ranges are shown in table 1. Note that R_λ decreases with increasing x/M for all mean speeds as can be seen in figure 7. The large-scale isotropy ratios, $I_{uv} = (\overline{u^2}/\overline{v^2})^{1/2}$ and $I_{vw} = (\overline{v^2}/\overline{w^2})^{1/2}$, can be seen in figure 8 as a function of downstream position. For $x/M < 70$, I_{uv} varies with downstream position. The data presented herein correspond to downstream locations

https://doi.org/10.1017/jfm.2017.47 Published online by Cambridge University Press

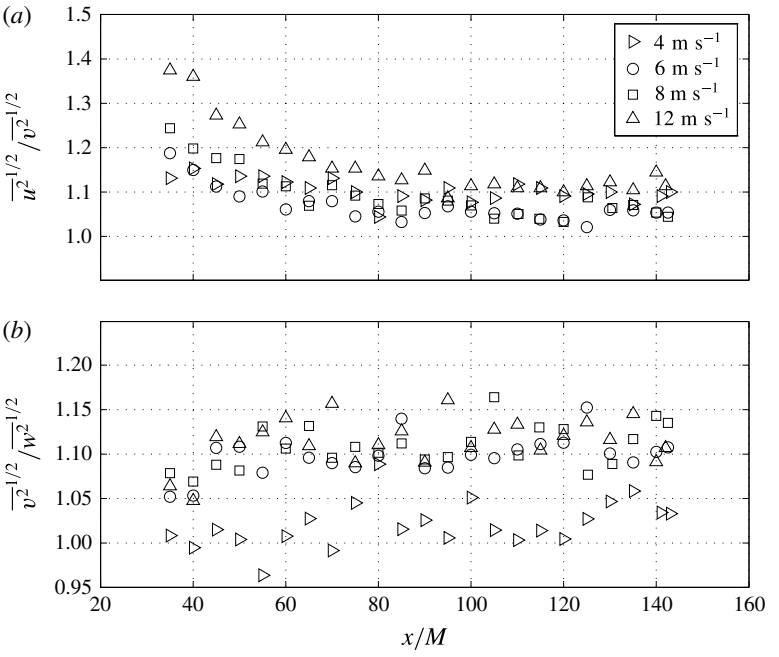


FIGURE 8. $I_{uv} = (\overline{u^2}/\overline{v^2})^{1/2}$ and $I_{vw} = (\overline{v^2}/\overline{w^2})^{1/2}$ as a function of downstream positon.

$\overline{U}$ (m s^{-1})	x/M	$I_{uv} = \left(\frac{\overline{u^2}}{\overline{v^2}}\right)^{1/2}$	$I_{uw} = \left(\frac{\overline{u^2}}{\overline{w^2}}\right)^{1/2}$	$I_{vw} = \left(\frac{\overline{v^2}}{\overline{w^2}}\right)^{1/2}$	R_{λ,u_u}
4	45–142	1.10 ± 0.019	1.12 ± 0.014	0.98 ± 0.015	191–303
6	55–142	1.05 ± 0.014	1.16 ± 0.014	1.11 ± 0.019	257–381
8	65–142	1.06 ± 0.018	1.18 ± 0.016	1.09 ± 0.020	366–482
12	80–142	1.12 ± 0.016	1.25 ± 0.013	1.10 ± 0.018	524–659

TABLE 1. Isotropy ratios and R_{λ,u_u} ranges.

where I_{uv} and I_{uw} vary less than 5 % from the isotropy ratios shown in table 1. The Taylor Reynolds number (R_{λ,u_u}) range at each mean velocity and the values for I_{uv}, I_{uw} and I_{vw} along with their standard deviations and the x/M locations used in this study are also shown in table 1. Note that the subscripts u_u and u_q denote, respectively, the use of $\overline{u^2}^{1/2}$ or $(q/3)^{1/2}$ as the characteristic velocity scale, i.e. $R_{\lambda,u_u} = \overline{u^2}^{1/2}\lambda/\nu$. The turbulence kinetic energy, q, is computed as

$$q = \overline{u^2} + \frac{1}{I_{uv}^2}\overline{u^2} + \frac{1}{I_{uw}^2}\overline{u^2}, \tag{4.1}$$

where $I_{uv} = (\overline{u^2}/\overline{v^2})^{1/2}$ and $I_{uw} = (\overline{u^2}/\overline{w^2})^{1/2}$ are the large-scale isotropy ratios. Since the standard deviation of the values for I_{uv} and I_{uw} are small, the average values are used in determining the turbulence kinetic energy.

One of the steps to determine C_ϵ is to identify the appropriate velocity scale, $\mathcal{U}$. The results presented herein use the two characteristic velocity scales identified

https://doi.org/10.1017/jfm.2017.47 Published online by Cambridge University Press

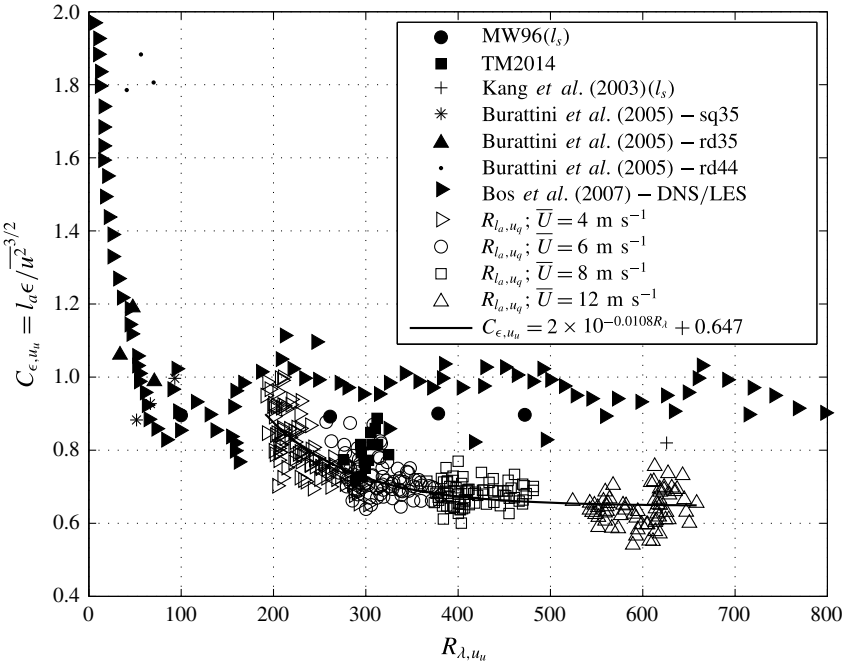


FIGURE 9. Comparison of C_{ϵ,u_u} versus R_{λ,u_u} for the current study to several active grid (MW96 (Mydlarski & Warhaft 1996), TM2014 (Thormann & Meneveau 2014), Kang, Chester & Meneveau (2003)), stationary grid (Burattini *et al.* 2005) and DNS (Bos *et al.* 2007) studies.

in (1.6) and (1.7) and apply them to the definition of C_ϵ, R_l and R_λ ((1.1), (1.3) and (1.4), respectively) in order to determine the effect on the value of C_ϵ. If the flow is isotropic, then the two characteristic velocity scales would lead to the same results. However, since the flow is slightly non-isotropic, the use of the two velocity scales will cause a shift in the values of R_λ, R_l and C_ϵ. The magnitude of the shift depends on the magnitude of the isotropy ratios shown in table 1.

Figure 9 shows C_{ϵ,u_u} as a function of R_{λ,u_u}. The solid line on that figure corresponds to an exponentially decaying least squares fit to the experimental data obtained in the present study. C_{ϵ,u_u} is seen to initially decrease with increasing R_{λ,u_u} and reaches a nearly constant value of $C_{\epsilon,u_u} = 0.65$ at $R_{\lambda,u_u} = 520$. The variation in C_{ϵ,u_u} at low values of R_{λ,u_u} is consistent with the stationary, bi-plane grid data presented by Burattini *et al.* (2005) and the DNS/LES (direct numerical simulation combined with large eddy simulation) data presented by Bos *et al.* (2007) as well as the stationary, bi-plane grid data from Valente & Vassilicos (2011) (not shown on plot). As found in other studies, C_{ϵ,u_u} becomes a constant at large values of R_{λ,u_u}. The constant value of C_{ϵ,u_u}, however, is lower than the active grid results reported by MW96 where $C_{\epsilon,u_u} = 0.9$, Kang *et al.* (2003) where $C_{\epsilon,u_u} = 0.82$ (obtained from Thormann & Meneveau 2014) and Thormann & Meneveau (2014) where $C_{\epsilon,u_u} = 0.80$ as well as the DNS/LES data reported by Bos *et al.* (2007) where $C_{\epsilon,u_u} = 0.92$ at similar values of R_{λ,u_u}. It is important to note that MW96 and Kang *et al.* (2003) use l_s (see § 3.2) as the measure of the integral scale for their experiments.

An alternative approach that can been used to determine C_ϵ is based on the analysis presented by Tennekes & Lumley (1972) as summarized by (1.2). This approach is

https://doi.org/10.1017/jfm.2017.47 Published online by Cambridge University Press

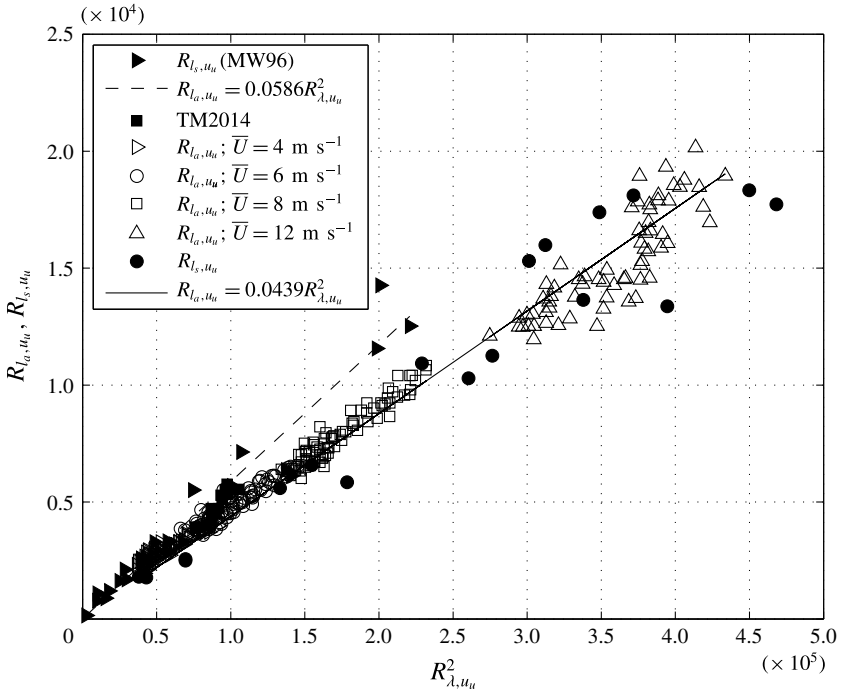


FIGURE 10. R_{l_a,u_u} versus R^2_{λ,u_u} and R_{l_s,u_u} versus R^2_{λ,u_u} for the current study, MW96 (Mydlarski & Warhaft 1996) and TM2014 (Thormann & Meneveau 2014). The solid line represents a linear least squares fit of the results obtained in the present study and the dashed line represents a linear least squares fit of the results obtained by MW96.

used by MW96 to find C_{ϵ,u_u} as it minimizes the scatter in the data. Other researchers (cf. Isaza *et al.* 2014 and Valente & Vassilicos 2011) present equivalent relation of l/λ as a function of R_λ (see (1.5)). Figure 10 shows a plot of R_{l_a,u_u} as a function of R^2_{λ,u_u} for results presented in MW96, Thormann & Meneveau (2014) and the present study. The solid and dashed lines represent linear least squares fits of the results for the present study and MW96, respectively. The least squares curve fits lead to a C_{ϵ,u_u} value of 0.66 (present study) and 0.88 (MW96), which are consistent with the values found from figure 9. Even though the value of C_{ϵ,u_u} varies at low values of R_{λ,u_u}, since the data include large values of R_{λ,u_u}, equation (1.2) leads to nearly the same value for C_{ϵ,u_u}.

There are two possible reasons for the difference between the C_{ϵ,u_u} value obtained by MW96 and the present study. The first is the definition of the integral scale used to compute C_{ϵ,u_u}. The present study primarily uses the autocorrelation method to compute the integral scale, l_a, while MW96 uses the peak of the energy spectrum to compute the integral scale, l_s. Burattini *et al.* (2005) show that the two definition are not necessarily interchangeable and the difference between l_a and l_s depends on the shape of the low wavenumber portion of the velocity power spectrum. In fact, they show that if $E_{11}(\kappa) \sim \kappa^4$ as $\kappa \to 0$ (the von Kármán spectrum), the difference between the two definitions of integral length scale is 10 %. A comparison of R_{l_a,u_u} versus R^2_{λ,u_u} and R_{l_s,u_u} versus R^2_{λ,u_u} is also shown in figure 10 for the present study. One of the main challenges in determining the integral scale, l_s, for the present study is that some spectra show a relative peak at 4 Hz due to the grid rotation that

https://doi.org/10.1017/jfm.2017.47 Published online by Cambridge University Press

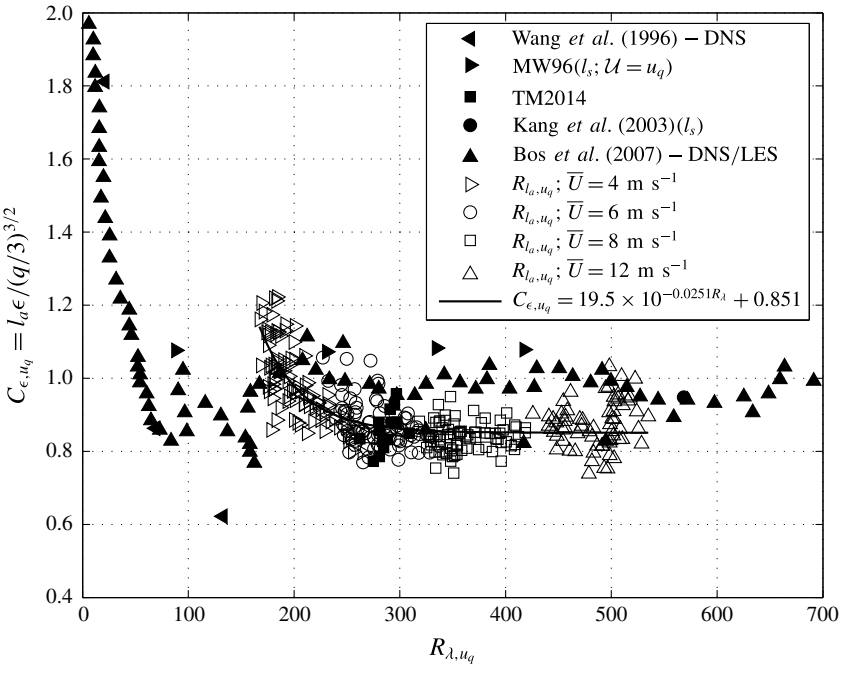


FIGURE 11. Comparison of C_{ϵ,u_q} versus R_{λ,u_q} for the current study to several active grid (MW96 (Mydlarski & Warhaft 1996), TM2014 (Thormann & Meneveau 2014), Kang *et al.* (2003)), stationary grid and DNS (Wang *et al.* 1996; Bos *et al.* 2007) studies.

coincides or obscures the peak of the energy spectrum that represents the integral scale (see figure 6). For most test conditions in the current study, the autocorrelations are not significantly affected by the relative peak at 4 Hz produced by the grid and, therefore, the integral length scale is primarily determined from the autocorrelation. Although there is notably more scatter in the measure of R_{l_s,u_u}, it is clear that R_{l_a,u_u} and R_{l_s,u_u} are in good agreement for the current study. In fact, a linear least curve fit of the R_{l_s,u_u} data in figure 10 leads to $C_{\epsilon,u_u} = 0.64$, which is consistent with the value found from the autocorrelation data. Although one could assume that a similar result would be obtained by MW96 since their active grid is very similar to the one used in the present study, the grid forcing protocol and tunnel geometry are different. This could cause differences in the large-scale characteristics and the shape of the energy spectrum in the low wavenumber range.

The second possible reason for the difference between the values of C_{ϵ,u_u} between the two studies is the difference in large scale isotropy found in the two flows. Bos *et al.* (2007) show that the value of C_{ϵ,u_u} will be different for homogeneous and isotropic decaying flows and flows with large-scale forcing. This means that the value of C_{ϵ,u_u} could vary depending on the lack of homogeneity or isotropy present in the flow since that could cause turbulence kinetic energy production. Figure 11 shows C_{ϵ,u_q} as a function of R_{λ,u_q}. The solid line on that figure corresponds to an exponentially decaying least squares fit to the data obtained in the current experiment. C_{ϵ,u_q} is seen to initially decrease with increasing R_{λ,u_u} and reaches a constant value of $C_{\epsilon,u_q} \approx 0.87$ at $R_{\lambda,u_q} = 305$. Figure 11 also shows the decaying, homogeneous and isotropic DNS/LES data reported by Bos *et al.* (2007) and DNS data from Wang *et al.* (1996) (obtained from Sreenivasan 1998) as well as the MW96 and TM2014

https://doi.org/10.1017/jfm.2017.47 Published online by Cambridge University Press

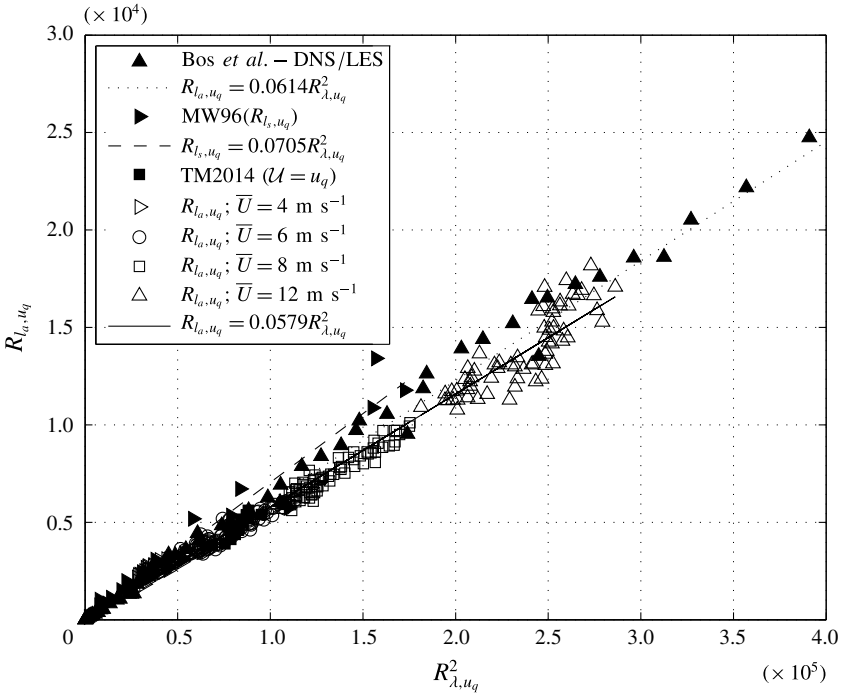


FIGURE 12. R_{l_a,u_q} versus R^2_{λ,u_q} for the current study, MW96 (Mydlarski & Warhaft 1996), TM2014 (Thormann & Meneveau 2014) and Bos *et al.* (2007). The solid line represents a linear least squares fit of the results obtained in the present study, the dashed line represents a linear least squares fit of the results obtained by MW96 and the dotted line represents a linear least squares fit of the results obtained by Bos *et al.* (2007).

data that have been corrected for anisotropy using (4.1). It is important to note that both MW96 and TM2014 do not report values for $\overline{w^2}^{1/2}$. Therefore it is assumed for those studies that $\overline{w^2}^{1/2} = \overline{v^2}^{1/2}$.

Figure 12 shows a plot of R_{l_a,u_q} as a function of R^2_{λ,u_q} for data reported by Bos *et al.* (2007), MW96, TM2014 and the present study. The solid, dashed and dotted lines represent a linear least squares fit for data obtained in the current study, MW96 and Bos *et al.* (2007), respectively. A summary of the results from the least squares curve fits can be seen in table 2, which shows that employing the isotropic correction to R_λ and R_{l_a} has moved the resulting C_ϵ from TM2014, Bos *et al.* (2007) and the present data much closer together. This signifies that the use of $(q/3)^{1/2}$, instead of $\overline{u^2}^{1/2}$, as the characteristic velocity scale might be more appropriate to determine values of R_λ, R_{l_a} and C_ϵ. It is important to point out that since it is assumed that $\overline{w^2}^{1/2} = \overline{v^2}^{1/2}$ for results reported by MW96 and TM2014, R_{l,u_q} and R_{λ,u_q} could be different from the true values, which could explain the increased difference in C_{ϵ,u_q} between MW96 and the other studies. The results shown in table 1 show that for moderate intensity, nearly homogeneous and isotropic flows, C_{ϵ,u_q} varies from 0.86 to 1.06 with an average value of about 0.93.

Identifying the location where the 'far-field' turbulence begins is of some importance since it appears that at this point the turbulence begins to follows the

https://doi.org/10.1017/jfm.2017.47 Published online by Cambridge University Press

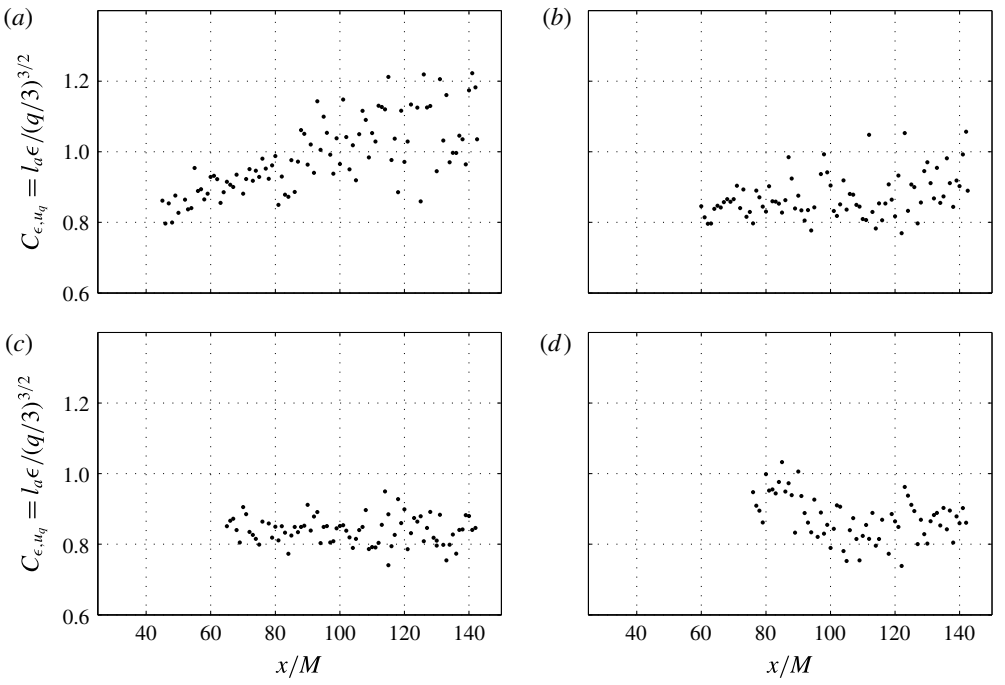


FIGURE 13. C_{ϵ,u_q} versus x/M for mean speeds of (*a*) 4 m s^{-1}, (*b*) 6 m s^{-1}, (*c*) 8 m s^{-1} and (*d*) 12 m s^{-1}.

—	I_{uv}	I_{uw}	C_{ϵ,u_u}	C_{ϵ,u_q}
MW96	1.21	—	0.9	1.06
Bos *et al.* (2007)	1.0	1.0	0.92	0.92
Kang *et al.* (2003)	1.16	—	0.82	0.95
TM2014	1.08	—	0.80	0.86
Current study	1.08	1.18	0.66	0.87

TABLE 2. Isotropy correction for different studies. Note that $(\overline{w^2})^{1/2}$ is not given for MW96, TM2014 and Kang *et al.* (2003), therefore it is assumed that $(\overline{w^2})^{1/2} = (\overline{v^2})^{1/2}$ for those studies.

Kolmogorov phenomenology described by a constant value of C_ϵ as suggested by Hearst & Lavoie (2014) and Isaza *et al.* (2014). Figure 13 shows C_{ϵ,u_q} as a function of normalized downstream position from the grid, x/M, for the mean speeds used in the present experiment. The $\overline{U} = 4$ m s^{-1} case shown in figure 13(*a*) shows that C_{ϵ,u_q} increases linearly with increasing values of x/M for the range, $45 \leqslant x/M \leqslant 90$, and appears to become a constant for $x/M > 90$. Figures 13(*b*) and 13(*c*), which correspond to $\overline{U} = 6$ m s^{-1} and 8 m s^{-1}, respectively, show that C_{ϵ,u_q} is constant with downstream position for values of x/M greater than approximately 60. This suggests that the extent of the 'near field' for active grids is not only dependent on grid geometry as suggested by Hearst & Lavoie (2014) for fractal grids, but also on other parameters such as mean speed.

https://doi.org/10.1017/jfm.2017.47 Published online by Cambridge University Press

5. Conclusion

Wind tunnel experiments are conducted in high intensity, homogeneous and nearly isotropic turbulence generated by means of an active turbulence grid modelled after the design proposed by Makita & Sassa (1991) as implemented by Mydlarski & Warhaft (1996). Time-resolved velocity measurements are obtained using a hot-wire anemometer for $191 \leqslant R_{\lambda,u_u} \leqslant 659$ in the far field of the active grid. The integral length scale is measured using two methods: integrating the longitudinal autocorrelation function to the first zero crossing (l_a) and by identifying the location of the peak of the energy spectrum (l_s) (Webb 1955; Pearson *et al.* 2002). It is found that R_{l_s} versus R_λ^2 and R_{l_a} versus R_λ^2 lead to a similar value of C_ϵ for the study presented herein suggesting that $l_s \approx l_a$. Since the forcing protocol of active grids can have a significant effect on the large scales of the flow (Hearst & Lavoie 2014), l_s may not equal l_a for all active grid flows since their relation is related to $E_{11}(\kappa) \sim \kappa^p$ for $\kappa \to 0$ (Burattini *et al.* 2005).

It is found that for sufficiently high R_λ values in a nearly homogeneous and isotropic flow downstream of an active grid, the normalized dissipation rate, C_ϵ is nearly independent of R_λ. The data presented here show that deviation from isotropy, even if small, could cause inconsistencies in the computation of R_l, R_λ and C_ϵ. It is suggested that C_{ϵ,u_q} rather than C_{ϵ,u_u} should be used when comparing nearly isotropic flows.

The method suggested by Tennekes & Lumley (1972) and Mydlarski & Warhaft (1996) that uses $R_l = (D_\infty/15)R_\lambda^2$ to find C_ϵ gives nearly the same value as computing C_ϵ directly using (1.1) as long as R_λ is large enough. C_{ϵ,u_q} obtained in the present study is in agreement with the active grid study of Thormann & Meneveau (2014) and the DNS/LES study of Bos *et al.* (2007), which suggests that $C_{\epsilon,u_q} = 0.9 \pm 0.02$. The discrepancy with the value of C_{ϵ,u_q} from data presented by Mydlarski & Warhaft (1996) could possibly be due to the definition of integral scale used (l_s), which may not be equal to the value obtained using the autocorrelation method (Burattini *et al.* 2005) and that $\overline{w^2}^{1/2}$ data are not provided, which could cause errors in the computation of C_{ϵ,u_q}.

Acknowledgements

The authors would like to thank T. Koster for his assistance in the data collection and thoughtful discussion, A. Kine for his extensive help with the development of electronic equipment used and J. Lewis for his helpful comments. We thank O. Goushcha for his help in the development of the active grid, L. Mydlarski and Z. Warhaft for their helpful suggestions early on in the project and M. Young for providing data used to calculate the uncertainty of the integral length scale computed using the autocorrelation measurements. Finally, we would like to acknowledge the reviewers for their constructive comments.

Appendix

The X-wire calibration is performed in the potential core of a laminar jet. The jet has the capability to vary the velocity and the angle of the X-wire in order to obtain 87 voltage pairs with velocities ranging from 2 to 24 m s^{-1} and an angle range of $\pm 33°$. The calibration equation used is a fourth-order polynomial that relates the voltage pairs to angle and velocity. The calibration is compared to test points taken in the laminar jet and it is found that $\overline{U}$ is accurate to within 1 % where $\overline{U}$ is the

https://doi.org/10.1017/jfm.2017.47 Published online by Cambridge University Press

mean velocity in the downstream direction. The velocity statistics obtained from the X-wire are also compared to statistics obtained from a standard single hot-wire. The downstream velocity intensity, $\overline{u^2}^{1/2}/\overline{U}$ where $\overline{u^2}^{1/2}$ is the downstream velocity r.m.s., obtained from the X-wire and a single hot-wire are found to differ by less than about 2 %. Further details can be found in Nguyen (2015).

REFERENCES

ANTONIA, R. A. & PEARSON, B. R. 2000 Effect of initial conditions on the mean energy dissipation rate and the scaling exponent. *Phys. Rev.* E **62** (6), 8086.

AZAD, R. S. 1993 Effects of hot-wire length and length-diameter ratio on spectral energy of turbulence. *Meas. Sci. Technol.* **4**, 405–410.

BOFFETTA, G. & ROMANO, G. P. 2002 Structure functions and energy dissipation dependence on Reynolds number. *Phys. Fluids* **14**, 3453–3458.

BOS, W. J., SHAO, L. & BERTOGLIO, J. P. 2007 Spectral imbalance and the normalized dissipation rate of turbulence. *Phys. Fluids* **19** (4), 045101.

BRUUN, H. H. 1995 *Hot-Wire Anemometry*. Oxford Science.

BURATTINI, P., LAVOIE, P. & ANTONIA, R. A. 2005 On the normalized turbulent energy dissipation rate. *Phys. Fluids* **17**, 98103.

CAO, N., CHEN, S. & DOOLEN, G. D. 1999 Statistics and structures of pressure in isotropic turbulence. *Phys. Fluids* **11**, 2235–2250.

CHAMPAGNE, F. H. 1978 The fine-scale structure of the turbulent velocity field. *J. Fluid Mech.* **86**, 67–108.

GOTO, S. & VASSILICOS, J. C. 2009 The dissipation rate coefficient of turbulence is not universal and depends on the internal stagnation point structure. *Phys. Fluids* **21**, 035104.

HEARST, R. J. & LAVOIE, P. 2014 Decay of turbulence generated by a square-fractal-element grid. *J. Fluid Mech.* **741**, 567–584.

HEARST, R. J. & LAVOIE, P. 2015 The effect of active grid initial conditions on high Reynolds number turbulence. *Exp. Fluids* **56** (10), 1–20.

HURST, D. & VASSILICOS, J. C. 2007 Scalings and decay of fractal-generated turbulence. *Phys. Fluids* **19** (3), 035103.

ISAZA, J. C., SALAZAR, R. & WARHAFT, Z. 2014 On grid-generated turbulence in the near-and far field regions. *J. Fluid Mech.* **753**, 402–426.

ISHIHARA, T. & KANEDA, Y. 2003 High resolution DNS of incompressible homogeneous forced turbulence-time dependence of the statistics. In *Statistical Theories and Computational Approaches to Turbulence*, pp. 177–188. Springer.

KANEDA, Y., ISHIHARA, T., YOKOKAWA, M., ITAKURA, K. I. & UNO, A. 2003 Energy dissipation rate and energy spectrum in high resolution direct numerical simulations of turbulence in a periodic box. *Phys. Fluids* **15**, L21.

KANG, H. S., CHESTER, S. & MENEVEAU, C. 2003 Decaying turbulence in an active-grid-generated flow and comparisons with large-eddy simulation. *J. Fluid Mech.* **480**, 129–160.

KROGSTAD, P. A. & DAVIDSON, P. A. 2011 Freely decaying, homogeneous turbulence generated by multi-scale grids. *J. Fluid Mech.* **680**, 417–434.

MAKITA, H. & SASSA, K. 1991 Active turbulence generation in a laboratory wind tunnel. *Advances in Turbulence 3*. pp. 497–505. Springer.

MAZELLIER, N. & VASSILICOS, J. C. 2008 The turbulence dissipation constant is not universal because of its universal dependence on large-scale flow topology. *Phys. Fluids* **20**, 15101.

MAZELLIER, N. & VASSILICOS, J. C. 2010 Turbulence without Richardson–Kolmogorov cascade. *Phys. Fluids* **22** (7), 075101.

MYDLARSKI, L. & WARHAFT, Z. 1996 On the onset of high-Reynolds-number grid-generated wind tunnel turbulence. *J. Fluid Mech.* **320**, 331–368.

NGUYEN, B. 2015. Calibration of an x-wire with assessment of a moderately high Reynolds number flow. Master's thesis, University of California, Irvine, CA.

https://doi.org/10.1017/jfm.2017.47 Published online by Cambridge University Press

NOBACH, H. & TROPEA, C. 2012 A statistical method for transforming temporal correlation functions from one-point measurements into longitudinal spatial and spatio-temporal correlation functions. *Exp. Fluids* **53**, 1815–1821.

PEARSON, B. R., KROGSTAD, P. A. & WATER, W. VAN DE 2002 Measurements of the turbulent energy dissipation rate. *Phys. Fluids* **14**, 1288–1290.

SEOUD, R. E. & VASSILICOS, J. C. 2007 Dissipation and decay of fractal-generated turbulence. *Phys. Fluids* **19**, 105108.

SREENIVASAN, K. R. 1984 On the scaling of the turbulence energy dissipation rate. *Phys. Fluids* **27**, 1048–1051.

SREENIVASAN, K. R. 1998 An update on the energy dissipation rate in isotropic turbulence. *Phys. Fluids* **10**, 528–529.

TENNEKES, H. & LUMLEY, J. L. 1972 *A First Course in Turbulence*. MIT Press.

THORMANN, A. & MENEVEAU, C. 2014 Decay of homogeneous, nearly isotropic turbulence behind active fractal grids. *Phys. Fluids* **26** (2), 025112.

VALENTE, P. C. & VASSILICOS, J. C. 2011 The decay of turbulence generated by a class of multiscale grids. *J. Fluid Mech.* **687**, 300–340.

VALENTE, P. C. & VASSILICOS, J. C. 2014 The non-equilibrium region of grid-generated decaying turbulence. *J. Fluid Mech.* **744**, 5–37.

VASSILICOS, J. C. 2015 Dissipation in turbulent flows. *Annu. Rev. Fluid Mech.* **47**, 95–114.

WANG, L. P., CHEN, S., BRASSEUR, J. G. & WYNGAARD, J. C. 1996 Examination of hypotheses in the kolmogorov refined turbulence theory through high-resolution simulations. Part 1. Velocity field. *J. Fluid Mech.* **309**, 113–156.

WEBB, E. K. 1955. Autocorrelations and energy spectra of atmospheric turbulencel. In *Div. of Meteorological Physics Technical Paper*. Australia: Commonwealth Scientific and Industrial Research Organization.

WYNGAARD, J. C. 1968 Measurement of small-scale turbulence structure with hot wires. *J. Phys.* E **1**, 1105.

YEUNG, P. K. & ZHOU, Y. 1997 Universality of the kolmogorov constant in numerical simulations of turbulence. *Phys. Rev.* E **56**, 1746.

https://doi.org/10.1017/jfm.2017.47 Published online by Cambridge University Press